Chemical Engineering Journal 382 (2020) 122825

Contents lists available at ScienceDirect

Chemical Engineering Journal

journal homepage: www.elsevier.com/locate/cej

Bimetallic metal-organic frameworks (MOFs) synthesized using the spray method for tunable CO_2 adsorption

Xiang He, Da-Ren Chen, Wei-Ning Wang*

Department of Mechanical and Nuclear Engineering, Virginia Commonwealth University, Richmond, VA 23219, United States

HIGHLIGHTS

- The microdroplet-based spray enables facile bimetallic MOFs manufacturing.
- Incorporation of secondary metal sites slightly increases the surface area.
- Pore volumes positively correlate with the atomic radii of secondary metal sites.
- Secondary metal sites alter gas sorption capacity, adsorption heat and selectivity.
- Geometry of adsorbed CO_2 depends on electronegativity of interacting metal sites.

GRAPHICAL ABSTRACT

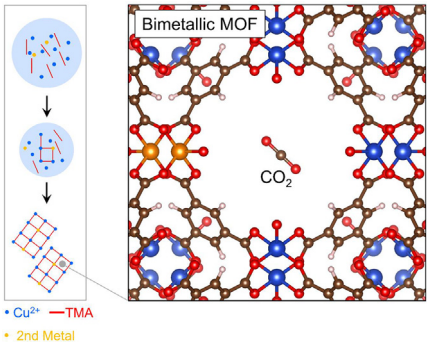

ARTICLE INFO

Keywords:
Microdroplet
Metal Substitution
Secondary Metal Sites
Electronegativity
Atomic Radius

ABSTRACT

A microdroplet-based spray process was applied for the fast and facile synthesis of a range of bimetallic metal–organic frameworks (MOFs), including Cu-TMA(Fe), Cu-TMA(Co), Cu-TMA(Mg), Cu-TMA(Al), and Cu-TPA(Fe) (TMA: trimesic acid; TPA: terephthalic acid). By forming M-O (M: metal, O: oxygen) bonds with the ligands, the secondary metal sites were incorporated into the framework partially substituting the original Cu sites in the parent MOF (i.e., Cu-TMA), which induced changes in surface areas, pore structures, and gas sorption properties. In particular, the bimetallic MOFs exhibited slightly higher surface areas than the parent MOF, which was attributable to the expansion of the unit cells, specifically because of the elongated M-O bonds. Meanwhile, the pore volumes of the MOFs showed a positive correlation with the atomic radii of the metal sites, suggesting that the metal substitution is an effective method to adjust the pore structures of the MOFs. Additionally, diverse gas sorption performances were observed among the bimetallic MOFs and the parent MOF, which was mainly associated with the different electrostatic interaction between the gas molecules and the frameworks induced by the incorporation of various secondary metal sites. Specifically, metal sites with larger electronegativity have a higher impact on the properties of the adsorbed CO_2, such as C═O bond length and O═C═O bond angle, leading to more asymmetric geometry and polarization of the adsorbed CO_2 molecules. As a result, the gas sorption capacity, selectivity, and isosteric heat of adsorption vary with various secondary metal sites inside the framework. The results from this work offer an alternative method for the rapid synthesis of bimetallic MOFs and add new aspects to the fundamental understanding of gas sorption using bimetallic MOFs.

* Corresponding author.
E-mail address: wnwang@vcu.edu (W.-N. Wang).

https://doi.org/10.1016/j.cej.2019.122825
Received 27 July 2019; Received in revised form 31 August 2019; Accepted 12 September 2019
Available online 12 September 2019
1385-8947/ © 2019 Elsevier B.V. All rights reserved.

Nomenclature

Abbreviations

NOAA	National Oceanic and Atmospheric Administration
CCS	carbon capture and storage
MOFs	Metal-organic frameworks
TMA	trimesic acid
DFT	density functional theory
TPA	terephthalic acid
DMF	dimethylformamide
DRIFTS	diffuse reflectance infrared Fourier transform spectroscopy
IAST	ideal adsorbed solution theory
CUS	coordinatively unsaturated metal sites
TSA	temperature swing adsorption

Symbols

p_t	total gas pressure
x	mole fraction of the adsorbed gas component
y	mole fraction of the gas component in bulk phase
q	adsorbed quantity
S	IAST selectivity
Qst	isosteric heat

1. Introduction

As a result of the heavy consumption of fossil fuels for the rising energy demands, the increasing anthropogenic carbon dioxide (CO_2) emission is becoming a prominent contributor to global climate change. Based on the data from the US National Oceanic and Atmospheric Administration (NOAA) [1], the CO_2 in atmosphere has reached ~415 ppm (May 2019), which is about 1.34 times that in 1960. To reduce atmospheric CO_2 concentration, it is vital to develop efficient materials for carbon capture and storage (CCS). Metal-organic frameworks (MOFs), a class of three-dimensional porous structure constructed with metals and organic ligands, have drawn huge attention for CCS [2,3], primarily due to their intriguing advantages, such as having a huge surface area, high porosity, and adjustable structure and functionality [4–6].

In general, CCS using MOFs is mostly governed by the interactions between CO_2 and MOFs, which can be affected by MOFs' properties, such as framework topology, framework charges, and ligand chemistry [7–10]. Taking MOF-74 for example, its excellent CO_2 adsorption performance mainly originated from strong Lewis acid and Lewis base interactions through both oxygen in CO_2 with metal ions and carbon in CO_2 with organic ligands [11], where the CO_2 binding strengths are tunable through adjusting the electrostatic interaction strengths by changing metal atoms [12]. By comparing CO_2 adsorption in ZIF-7, -11, -93, and -94, which are built with the same metals and ligands but with various topologies, pioneers pointed out the crucial role of topology in CO_2 adsorption [13]. More specifically, at low pressures (< 1 bar), higher CO_2 adsorption was observed with ZIF possessing smaller pores (i.e., ZIF-7 and 94 with sodalite (sod) topology) rather than the counterparts (i.e., ZIF-11 and -93, respectively; right half-open interval (rho) topology). While at higher pressures, the scenario of CO_2 adsorption was reversed [13]. The adsorption of CO_2 by MOFs can also be influenced by environmental conditions, such as the presence of water [14].

To further improve the adsorption capacity and selectivity of CO_2 molecules by MOFs, numerous strategies have been explored and developed, such as ligand functionalization [15], framework interpenetration [16], metal insertion [17], cation exchange [18], and substitution of metal ions in MOFs [19]. Among these strategies, metal ion substitution has recently drawn mounting attention, through which bimetallic MOF structures can be created via either direct synthesis or post-synthetic modification (PSM) [20]. Typical examples of the bimetallic MOF structures include MOF-74(Zn/Co) [21], MOF-5(Zn/Co) [22], MIL-53(Cr/Fe) [23], MOF-199(Cu/Ru) [24], ZIF-8(Zn/Cu) [25], and POST-65(Mn/Cu) [26]. In general, the partial metal substitution by a secondary metal ion induces variations in porous structures and adsorptive sites, which could subsequently affect the gas adsorption properties [20]. For example, bimetallic MIL-101 was prepared via partial substitution of Cr with Mg, where homogeneous dispersion of Mg was achieved in the framework through the coordination with the ligand (i.e., terephthalic acid) by forming Mg-O bonds [27]. The substituting Mg ions enhanced both CO_2 adsorption capacity and CO_2/N_2 adsorption selectivity by 40% and ~4 times, respectively [27]. The major reason for such an improvement was ascribed to the increased surface area and additional CO_2 adsorption sites after the Mg substitution. Notably, judicious selection of the substituting metal is also of great importance. Given the vast amount of existing MOF structures, various scenarios and mechanisms of CO_2 adsorption are expected for the bimetallic MOFs. Therefore, further efforts are still in need to contribute to the full understanding of CO_2 adsorption in bimetallic MOFs.

Here in this work, the Cu ions in the representative MOF, Cu-TMA (also called HKUST-1, TMA: trimesic acid), were partially substituted with other metal ions (i.e., Fe, Mg, Co, and Al) using a microdroplet-based spray system. In particular, this spray method enables the synthesis process to occur inside microdroplets, where the heat and mass transfer would be greatly enhanced [28], providing more thorough mixing of the precursors and ultimately leading to the homogeneous dispersion of the secondary metal sites inside the bimetallic MOFs. As demonstrated here, this method would offer an alternative and highly facile route for the rapid synthesis of bimetallic MOFs. Subsequently, systematic characterization was conducted to understand the mechanism of metal substitution using this process. Results showed that, the introduced secondary metal ions would substitute the Cu ions and form M-O bonds (M: metal, O: oxygen) with the ligand. Both the

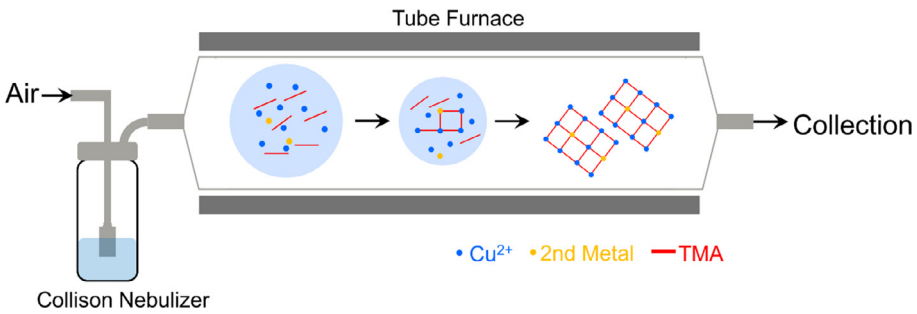

Scheme 1. Schematic illustration of the microdroplet-based spray process for the synthesis of Cu-TMA with *in situ* metal substitution.

amount and species of the substituting metal ions affect the properties and performances of the bimetallic MOFs. With the proper degree of metal substitution, the as-prepared bimetallic MOFs maintained the crystalline structure of the parent MOF. Whereas, an excessive amount of secondary metal ions would impair the structural integrity by interacting with the ligand which impedes the coordination between Cu^{2+} and the ligand. In particular, the presence of the secondary metal sites would slightly improve surface areas of the as-resulting bimetallic MOFs, which might be due to the expansion of the unit cells. Additionally, the pore volumes of the bimetallic MOFs increase with the atomic radii of the secondary metals. CO_2 and N_2 sorption measurements were carried out, from which the effects of secondary metal sites on gas sorption were analyzed together with density functional theory (DFT) simulations. Notably, the electronegativity of the secondary metals was found to be vital to CO_2 adsorption. Overall, this work will shed light on both the synthesis route for bimetallic MOFs and dependence of CO_2 adsorption on the secondary metal sites in bimetallic MOFs.

2. Materials and methods

2.1. General synthesis process

All the samples in this study were fabricated by using a microdroplet-based spray process. As shown in Scheme 1, the spray process consists of an air supply system, a Collision nebulizer (6-jet), a tube furnace (length: 1 m, inner diameter: 20 mm), and a glass fiber filter (EPM 2000, Whatman™) for sample collection. Typically, a precursor solution containing metal ions and organic ligands is atomized into microdroplets, which are subsequently carried by air flow (5 L/min) through the tube furnace (200 °C for all samples except for Cu-TPA(Fe) (TPA: terephthalic acid), where 100 °C was used). Inside the tube furnace, the solvent evaporates, and the chemicals undergo nucleation and crystallization. Finally, the samples were collected by the glass fiber filter. The details of the precursor compositions are listed in Table 1.

2.2. Sample washing procedures

After their synthesis, all samples were scraped off the filter and subjected to a dispersion-centrifugation process to remove residuals. More specifically, Cu-TMA and Cu-TMA(Mg, Fe, and Co) were washed with DMF twice followed by methanol once, while Cu-TPA(Fe) was washed with DMF three times. The Cu-TMA(Al) was firstly washed with DMF/DI water mixture (vol/vol = 2:1) twice and then methanol once. All the samples were finally dried in the vacuum oven at 50 °C.

2.3. Material characterization

The elemental analysis of the samples was conducted using energy-dispersive X-ray spectroscopy (EDX, Su-70, Hitachi). The powder X-ray diffraction (PXRD) patterns were obtained from an X-ray diffractometer (X'Pert PRO, PANalytical). Nicolet iS50 (Thermo Scientific) was used to collect the Fourier transform infrared (FT-IR) spectra. X-ray photoelectron spectroscopy (XPS) measurements were conducted by using a scanning XPS microprobe (PHI VersaProbe III). Thermogravimetric Analysis (TGA) was performed using TA Q500 under N_2 flow with a heating rate of 10 °C/min. The gas adsorption experiments were carried out using Autosorb iQ (Quantachrome Instruments).

2.4. Dynamic CO_2 adsorption

In situ diffuse reflectance infrared Fourier transform spectroscopy (DRIFTS) was carried out to study the characteristics of adsorbed CO_2 molecules and CO_2 adsorption kinetics under the dynamic flow conditions. Detailed procedures have been reported in a prior study.[29]

2.5. Computational methods

All density functional theory (DFT) calculations were conducted with CP2K [30] (version: 6.1) using the Quickstep module. In particular, Perdew-Burke-Ernzerhof (PBE) function [31] was applied here with semiempirical dispersion corrections (DFT-D3) [32]. The double-ζ Gaussian-type basis set (DZVP-MOLOPT) [33] was used for metal atoms, while triple-ζ Gaussian-type basis set (TZVP-MOLOPT) [33] was employed for all other atoms. Goedecker-Teter-Hutter (GTH) pseudopotentials [34] were adopted here for all atoms. All calculations were carried out with the primitive cell (Scheme 2B), which was derived from the unit cell (Scheme 2A).

3. Results and discussion

3.1. Material characterization

As the first demonstration of the *in situ* metal substation via the microdroplet-based spray process, a series of Cu-TMA(Fe) samples were prepared by adjusting the molar ratios of Fe^{2+} to Cu^{2+} in the precursor solutions from 0 to 1 (Fig. 1A). As shown in Fig. 1B-I, with increasing Fe/Cu ratios, the color of Cu-TMA(Fe) was gradually tuned from blue to yellow, indicating the successful substitution of Fe^{2+} with partial Cu^{2+} inside the frameworks. Despite the color variations, both Cu-TMA(Fe) samples synthesized with the least and highest Fe^{2+} amount exhibited spherical shape (Fig. S1), the same shape of the parent Cu-TMA as reported in our prior study [35], which arose from the conversion of one droplet to one particle in a typical microdroplet-based spray system [36].

Further characterization of the as-prepared samples was conducted, and detailed results are shown in Fig. 2. More specifically, the EDX spectra (Fig. 2A) show that increasing the amount of $FeCl_2{\cdot}4H_2O$ in the precursor solution will lead to a gradual increase of the Fe peak, but consequently also leads to a decrease of the Cu peak intensity. Based on the EDX spectra, the Fe/Cu ratios in the products were derived and presented as a function of Fe/Cu ratios in the precursors (Fig. 2B). The results showed that changing the Fe/Cu ratios in the precursor (mol/mol, with fixed amount of Cu ions) from 0.1 to 1 led to the variations of Fe/Cu ratios in products from 0.3 to 15.1, indicating that the percentage of exchanged Cu in Cu-TMA(Fe) was tunable by simply adjusting the amount of $FeCl_2{\cdot}4H_2O$ in the precursor solution. The discrepancy in Fe/Cu ratios between precursors and products might be ascribed to the

Table 1
Precursor Compositions.

Samples	Solvents/mL		Ligands/g		$Cu(NO_3)_2{\cdot}3H_2O$/g	Secondary Metal Ions/g	
Cu-TMA	DMF	30	TMA	0.1261	0.2174	N/A	N/A
Cu-TMA(Fe)	DMF	30	TMA	0.1261	0.2174	$FeCl_2{\cdot}4H_2O$	0.0179–0.1789
Cu-TMA(Mg)	DMF	30	TMA	0.1261	0.2174	$MgCl_2$	0.0086
Cu-TMA(Co)	DMF	30	TMA	0.1261	0.2174	$Co(NO_3)_2{\cdot}6H_2O$	0.2619
Cu-TMA(Al)	DMF/DI	30/15	TMA	0.1261	0.2174	$Al_2(SO_4)_3{\cdot}H_2O$	0.0308
Cu-TPA(Fe)	DMF	30	TPA	0.0997	0.2174	$FeCl_2{\cdot}4H_2O$	0.0269

Notes: TMA: Trimesic Acid; TPA: Terephthalic Acid; DMF: Dimethylformamide; DI: Deionized Water.

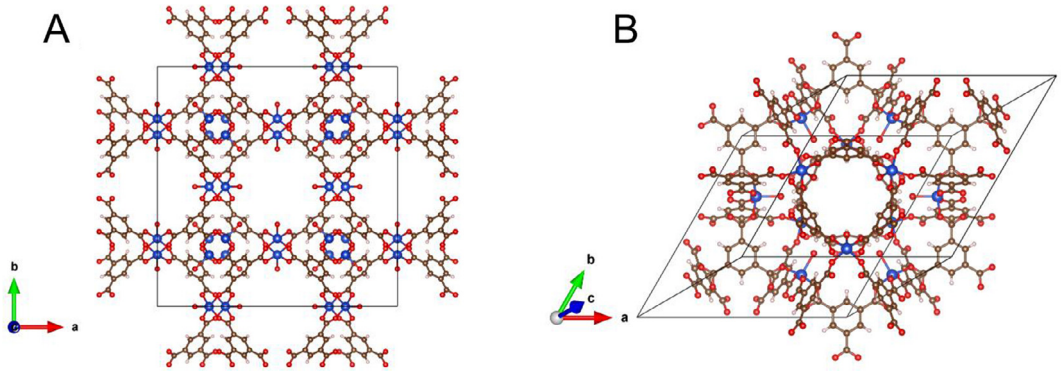

Scheme 2. Unit cell (A) and primitive cell (B) of Cu-TMA.

variations between Cu-TMA crystallization rate and Fe^{2+} substitution rate (or in other words, varying preference for the TMA to interact with Cu^{2+} and Fe^{2+}) [37]. The structural integrities of the samples were investigated with PXRD measurements. As exhibited in Fig. 2C, Cu-TMA remained structurally intact with low Fe/Cu ratios (0.1–0.4) in the precursors but started to become amorphous with Fe/Cu ratios over 0.4. These structural changes were attributable to the effects of Fe substitution on the coordination of Cu with TMA as evidenced by the FT-IR spectra (Fig. 2D). For the pure Cu-TMA, several dominant IR peaks were observed at 760 cm^{-1}, 1370 cm^{-1}, and 1445 cm^{-1}, which could be assigned to Cu—O bond, symmetric and asymmetric vibration of TMA carboxylate groups, respectively [38–41]. The peak at 728 cm^{-1} also corresponds to the Cu—O bond, formed through the coordination of Cu ions with TMA [42]. Notably, the intensity of this IR peak (i.e., Cu—O) decreased with the increased extent of Fe substitution. Meanwhile, a new peak appeared at 710 cm^{-1}, corresponding to the Fe—O bond [43]. This result suggested that the excessive Fe ions would interact with TMA and thus impede the coordination of Cu with TMA to form Cu-TMA crystalline structure. Excessive Fe ions also led to additional peaks at 610 cm^{-1}, which can be assigned to —OH in TMA [44]. This provided further evidence of poor coordination between TMA and Cu due to the perturbation of excessive Fe ions. Meanwhile, the current synthesis parameters (e.g., temperature and reaction time) were designed for Cu-TMA and are unfavorable for the formation of three-dimensional Fe-TMA framework, which explains the amorphous structure at high Fe/Cu ratios in precursors (Fig. 2C).

The chemical states of the elements in Cu-TMA and Cu-TMA(Fe) were also studied using XPS. As shown in Fig. 3A, both samples exhibited similar survey spectra, where dominant peaks of C1s and O1s were clearly identified at 285 eV and 532 eV, respectively. To further analyze the effects of Fe substitution on the chemical states of elements in Cu-TMA, high-resolution XPS spectra of Cu2p, O1s, and Fe2p were obtained (Fig. 3B-D). As shown in Fig. 3B, the element of Cu in pristine Cu-TMA showed a peak at ~935 eV and two peaks between 938 eV and 948 eV, corresponding to the $Cu2p_{3/2}$ main peak and satellite peaks, respectively [45]. In the case of Cu-TMA(Fe), marginal difference was observed for $Cu2p_{3/2}$ in terms of peak positions and relative ratios, which might be caused by various coordination environments as

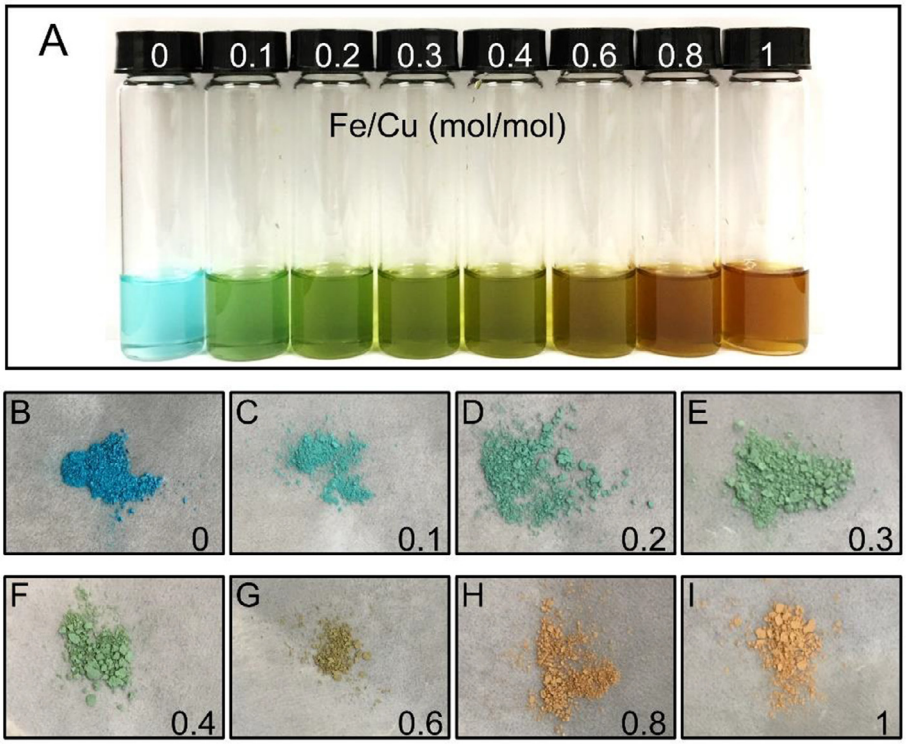

Fig. 1. (A) Images of the Cu-TMA(Fe) precursors with various Fe/Cu ratios. Images of Cu-TMA(Fe) synthesized with increasing Fe/Cu ratios (mol/mol) in the precursors: (B) 0; (C) 0.1; (D) 0.2; (E) 0.3; (F) 0.4; (G) 0.6; (H) 0.8; (I) 1.

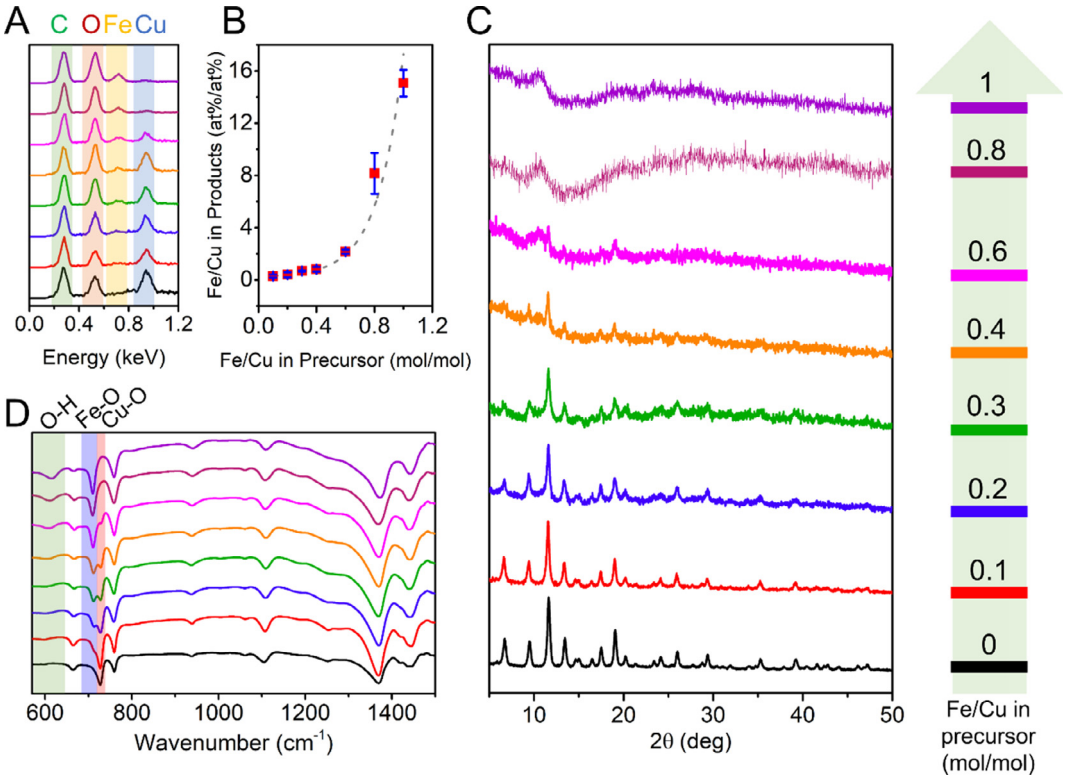

Fig. 2. (A) EDX spectra of Cu-TMA(Fe) samples; (B) The Fe/Cu ratios in Cu-TMA(Fe) as a function of the Fe/Cu ratios in precursors; (C) Powder X-ray diffraction (PXRD) patterns and (D) FT-IR spectra of Cu-TMA(Fe) samples (From bottom to top: the Fe/Cu ratios in precursors increased from 0 to 1; Note: the amount of Cu ions was fixed in the precursors).

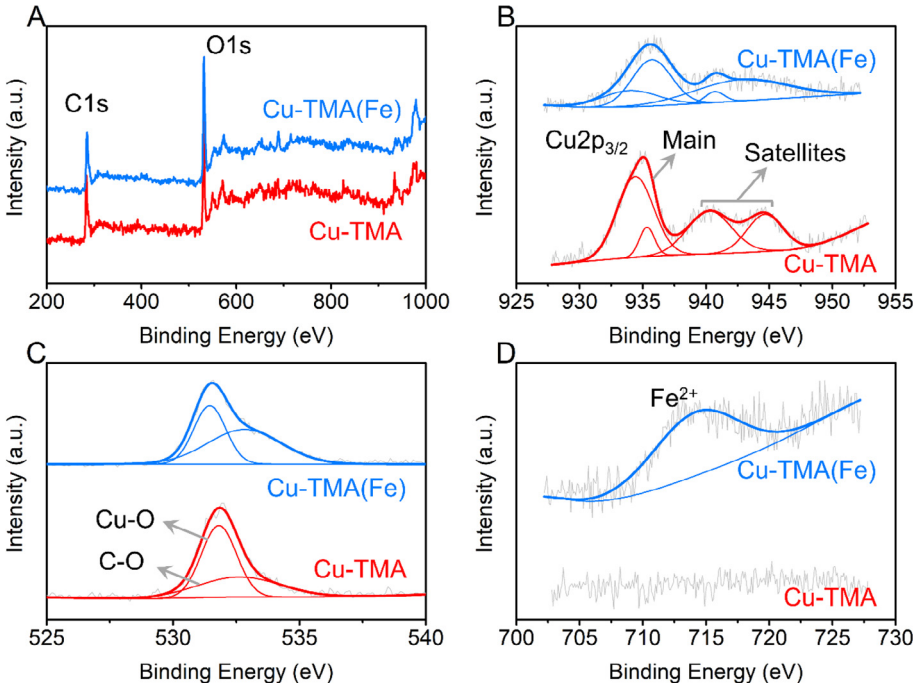

Fig. 3. XPS spectra of Cu-TMA and Cu-TMA(Fe) (Note: The Fe/Cu ratio in the precursor for this Cu-TMA(Fe) is 0.3.) (A) Survey spectra; High-resolution spectra of (B) Cu2p, (C) O1s, and (D) Fe2p.

induced by the presence of secondary metal sites. Fig. 3C shows the high-resolution spectra of O1s in both Cu-TMA and Cu-TMA(Fe). Both samples have two peaks at around 531.8 eV and 533.1 eV, attributed to O in metal clusters and carboxylates in TMA, respectively [46,47]. Notably, the ratios of the fitted peaks of O1s also varied between Cu-TMA and Cu-TMA(Fe), which once again suggests that the changes in the coordination environment were induced by Fe substitution. The high-resolution Fe2p spectra are shown in Fig. 3D. As expected, no peaks were observed between 705 eV and 725 eV for Cu-TMA. While an apparent peak showed up at 714.6 eV for Cu-TMA(Fe), demonstrating

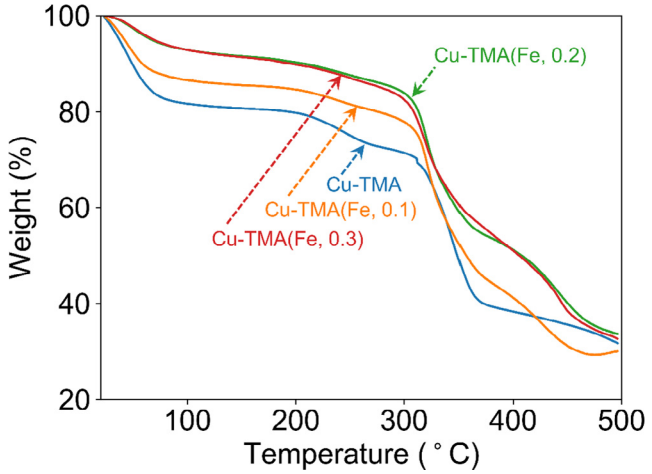

Fig. 4. TGA results of Cu-TMA and Cu-TMA(Fe) samples. Note: the numbers in parentheses refer to the Fe/Cu ratios in precursors.

the successful substitution of Fe in Cu-TMA, which is consistent with the results shown in Fig. 2.

The effects of Fe substitution on the thermal stability of Cu-TMA were explored with TGA. As shown in Fig. 4, the pristine Cu-TMA exhibited three stages of weight loss. The initial loss, at temperatures below 80 °C, corresponds to the removal of guest molecules (e.g., water). The gradual weight loss between 80 and 300 °C is probably due to the release of bounded molecules. The structure of the pristine Cu-TMA is stable up to 300 °C, after which the decomposition of linker begins. Similar TGA profiles were observed for the Cu-TMA(Fe) samples, all of which maintained their structural integrities up to 300 °C, demonstrating that partial Fe substitution does not affect the thermal stability of Cu-TMA. Interestingly, with the increasing substitution of Cu with Fe, less weight loss was observed at the initial stage, indicating that Fe substitution can decrease the adsorption of guest molecules (e.g., water), which to some extent is better for the structural integrity as Cu-TMA is vulnerable to excessive moisture [48].

In addition to Fe ions, the spray process is also applicable to substituting the Cu ions in Cu-TMA with other species, such as Mg, Co, and Al. As demonstrated in Fig. 5A, these metal elements were clearly identified in the EDX spectrum, indicating the successful substitution of Cu with these metal species. The PXRD patterns of these samples were presented in Fig. 5B, which showed that the crystalline structure of Cu-TMA was still intact after the substation with these metals. Besides Cu-TMA, the spray process for metal substitution also applies to other MOFs. Here, as a demonstration, we successfully synthesized Fe-substituted Cu-TPA as shown in Fig. 5.

3.2. Surface areas and pore structures

In order to understand the effects of secondary metal sites on the gas adsorption, four of the as-synthesized samples were selected and subjected to detailed sorption analysis, including Cu-TMA, Cu-TMA(Fe), Cu-TMA(Co), and Cu-TMA(Mg). In particular, the surface areas and porous structures of the samples were analyzed with nitrogen sorption isotherms at 77 K (Fig. 6A). As shown in Fig. 6A, all of the samples showed similar nitrogen sorption isotherms. The sharp increase at low relative pressures ($P/P_0 < 0.01$) originating from the continuous filling of micropores (pore width < 2 nm), which demonstrated the domination of microporous structures in all samples. The increase at high relative pressures and the evident hysteresis arise from pore condensation, which is the transition of gas to the liquid-like phase in pores and indicates the existence of mesoporous structures. The pore size distributions were determined using density functional theory and agree well with the information obtained from the nitrogen sorption isotherms. As presented in Fig. 6B, the as-prepared Cu-TMA exhibits characteristic pore widths at 1.6 and 3.8 nm. With the substitution of Cu with other metal ions, the overall pore structures were maintained with minor changes (Fig. 6B). In particular, the pore size was still dominated by ~1.6 nm while several additional pores showed up with sizes larger than 1.6 nm, demonstrating the coexistence of microporous and mesoporous structures. The Brunauer–Emmett–Teller (BET) surface areas of Cu-TMA, Cu-TMA(Mg), Cu-TMA(Fe), and Cu-TMA(Co) were calculated to be 930 m^2/g, 1462 m^2/g, 1487 m^2/g, and 1341 m^2/g, respectively (Fig. 6C). Interestingly, the surface area of the Cu-TMA became slightly larger after the metal substitution. The pore volumes of the samples were derived using the DFT method, and results were also shown in Fig. 6C. Notably, the pore volumes of the frameworks exhibit a positive relationship with the radii of the substituting metal atoms. Specifically, the atomic radii of Fe, Cu, Mg, and Co are 126 pm, 128 pm, 173 pm, and 200 pm, respectively. Correspondingly, the pore volumes of Cu-

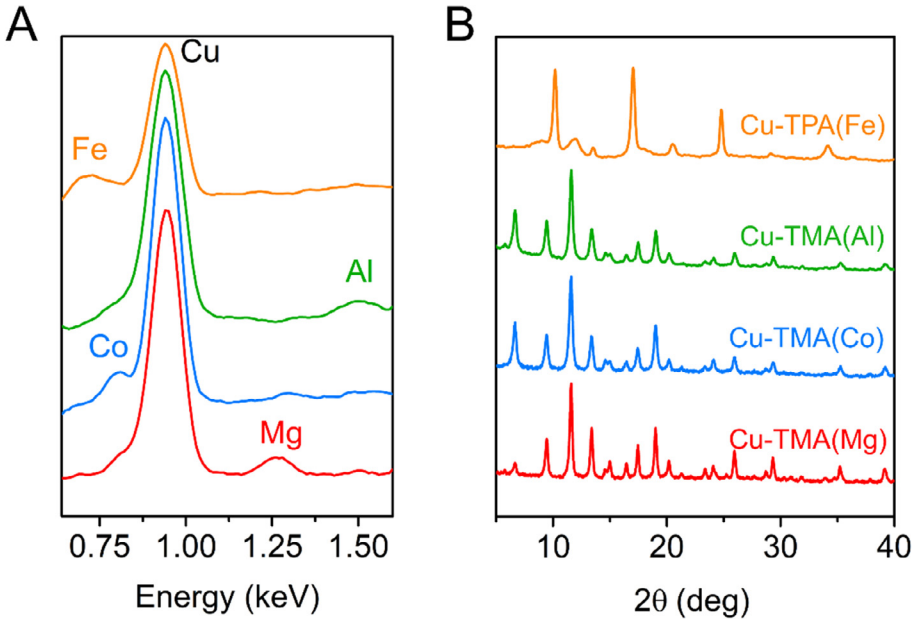

Fig. 5. (A) EDX spectra and (B) PXRD patterns of Cu-TPA(Fe), Cu-TMA(Al), Cu-TMA(Co) and Cu-TMA(Mg).

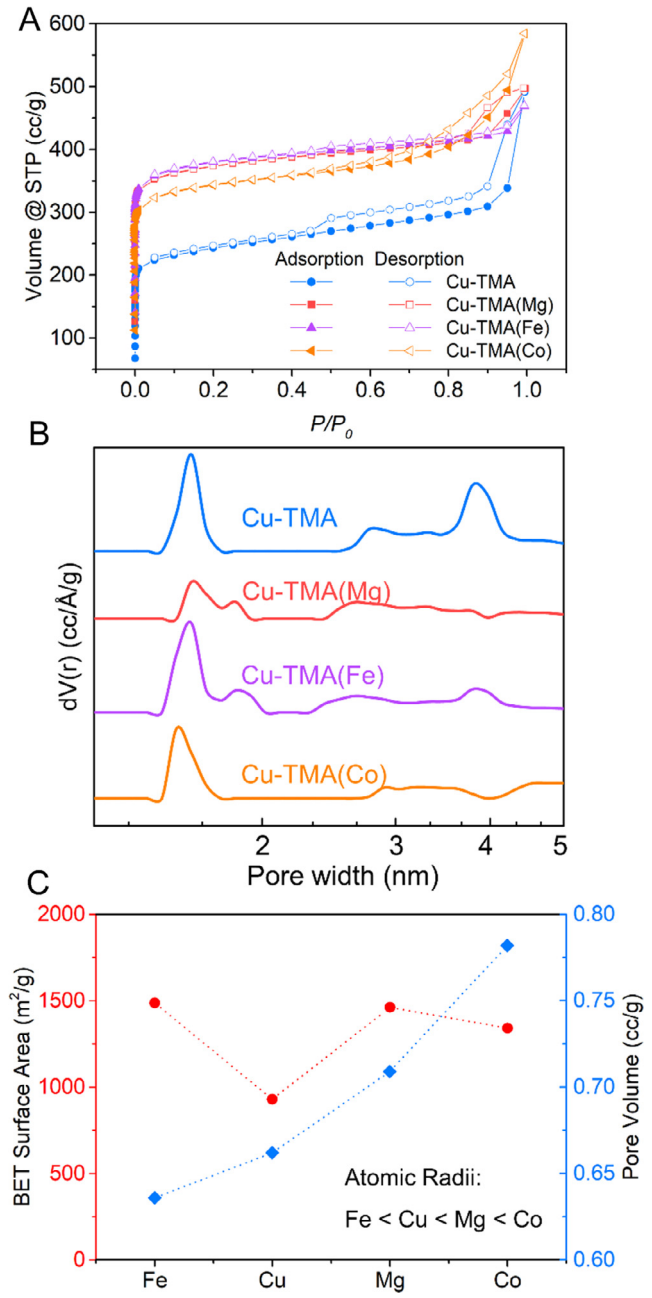

Fig. 6. (A) Nitrogen sorption isotherms (77 K); (B) Pore size distributions calculated with density functional theory (NLDFT-N_2-carbon equilibrium transition kernel (77 K) using a slit-pore model.); (C) BET surface areas and DFT pore volumes (x axis: Fe: Cu-TMA(Fe); Cu: Cu-TMA; Mg: Cu-TMA(Mg); Co: Cu-TMA(Co)).

TMA(Fe), Cu-TMA, Cu-TMA(Mg), and Cu-TMA(Co) show the same increasing trend with values of 0.636 cc/g, 0.662 cc/g, 0.709 cc/g, and 0.782 cc/g, respectively. The changes in both pore structure and surface area of the framework are attributable to the unit cell expansion, which was a result of the increased average length of the metal-oxygen bond after the metal-substitution process [49]. For instance, the average lengths of the Co-O and Fe-O bonds are 2.08 Å and 2.00 Å, respectively, both of which are larger than that of the Cu—O bond (i.e., 1.70 Å), eventually leading to the expansion of the unit cell of Cu-TMA(Co) and Cu-TMA(Fe) by 0.043 Å and 0.019 Å as compared to that of Cu-TMA [49].

3.3. Gas sorption analysis

The in-framework metal substitution plays a significant role in altering the gas sorption behaviors of MOFs. To further elucidate this, the sorption isotherms of two different gases (i.e., N_2 and CO_2) were measured at 273 K and 298 K. As shown in Fig. 7, all the isotherms exhibit reversible adsorption–desorption processes. More specifically, Cu-TMA adsorbed 3.0 mmol/g and 4.8 mmol/g of CO_2 at (298 K, 1 bar) and (273 K, 1 bar), respectively (Fig. 7A and B). With the partial substitution of Cu with Co, Fe, and Mg atoms, the capacity towards CO_2 adsorption (298 K and 1 bar) of the modified structures was improved to 3.7, 4.4, and 4.2 mmol/g, respectively. This improvement in CO_2 adsorption also stands at 273 K. In the case of N_2 adsorption, Cu-TMA and Cu-TMA(Co) showed similar N_2 adsorption isotherms at both 298 K and 273 K (Fig. 7C and D). While, the substitution of Cu with Fe and Mg atoms slightly improved the N_2 adsorption capacity of the structures.

To gather further insight, the adsorption selectivity of the CO_2/N_2 gas mixture (15% CO_2 and 85% N_2, mimicking flue gas composition [50]) was analyzed on the basis of the pure-component adsorption isotherms (Fig. 7) using the ideal adsorbed solution theory (IAST) [51]. Detailed simulation procedures are available in a prior study [52]. Briefly, the isotherms of N_2 and CO_2 were fitted with single-site and dual-site Langmuir-Freundlich models, respectively. Then, the mole fractions of the adsorbed gases were calculated using Eq. (1) with the fitting parameters, after which, the adsorption selectivity factors were predicted using Eq. (2).

$$\int_0^{p_t \cdot \frac{y_{CO_2}}{x_{CO_2}}} \frac{q_{CO_2}}{p_t} dp = \int_0^{p_t \cdot \frac{y_{N_2}}{x_{N_2}}} \frac{q_{N_2}}{p_t} dp \quad (1)$$

$$S = \frac{x_{CO_2}/y_{CO_2}}{x_{N_2}/y_{N_2}} \quad (2)$$

where, p_t stands for total gas pressure (bar); x represents the mole fraction of the adsorbed gas component; y is the mole fraction of the gas component in bulk phase; q is the adsorbed quantity (mmol/g); S represents the IAST selectivity.

As shown in Fig. 8, different scenarios for CO_2/N_2 selectivity were found with various bimetallic MOFs, owing to the deviations in crystalline structures and distinct secondary metal sites, while only weak dependence of selectivity on pressure was observed. Specifically, at 273 K, Cu-TMA, Cu-TMA(Mg) and Cu-TMA(Fe) showed subtle decreases in CO_2/N_2 selectivity with an increasing pressure load, while Cu-TMA(Co) exhibited slightly decreasing selectivity at low pressure loading followed by increasing selectivity at a high pressure loading regime. In particular, selectivity factors for Cu-TMA ranged from 16.2 to 18.3, which are higher than those for Cu-TMA(Mg) (i.e., 13.8–14.8) and Cu-TMA(Fe) (i.e., 14.0–16.0). For Cu-TMA(Co), with increasing loading pressure, the CO_2/N_2 selectivity factors initially decreased from 17.2 to 16.0, and then increased up to 16.5 at 1.0 bar. At 298 K, all structures showed increasing CO_2/N_2 selectivity at higher pressure loading. Specifically, Cu-TMA(Fe) showed the highest adsorption selectivity of CO_2 over N_2, followed by Cu-TMA, Cu-TMA(Co), and Cu-TMA(Mg). From pure gas isotherms, Henry's law constants were determined from the initial slopes, the ratios of which could be also used to compare the CO_2/N_2 selectivity (i.e., so-called initial slope calculation). As shown in Table S1, the CO_2/N_2 selectivity calculated based on the initial slopes was roughly consistent with the IAST data.

To gain insight of the CO_2 adsorption in these structures, the dependence of the isosteric heat (Qst) on CO_2 loading was analyzed with pure-gas sorption isotherms (Fig. 7) using the Clausius-Clapeyron equation [52]. As shown in Fig. 9, all four structures exhibited different Qst values and distinctive patterns at various CO_2 loadings. More specifically, with the initial CO_2 loadings, the Qst of CO_2 adsorption in the Cu-TMA approached 25.7 kJ/mol, which was larger than those in the Cu-TMA(Fe) (24.5 kJ/mol), Cu-TMA(Mg) (23.2 kJ/mol), and Cu-

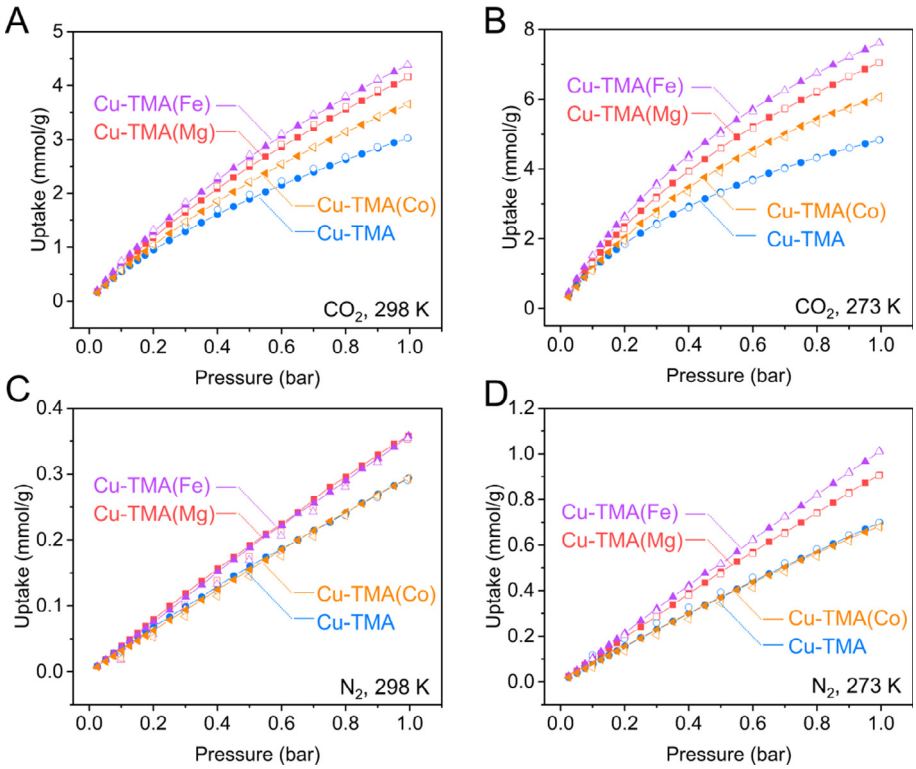

Fig. 7. Adsorption (filled scatters) and desorption (empty scatters) isotherms measured with (A) CO_2 at 298 K, (B) CO_2 at 273 K, (C) N_2 at 298 K, and (D) N_2 at 273 K.

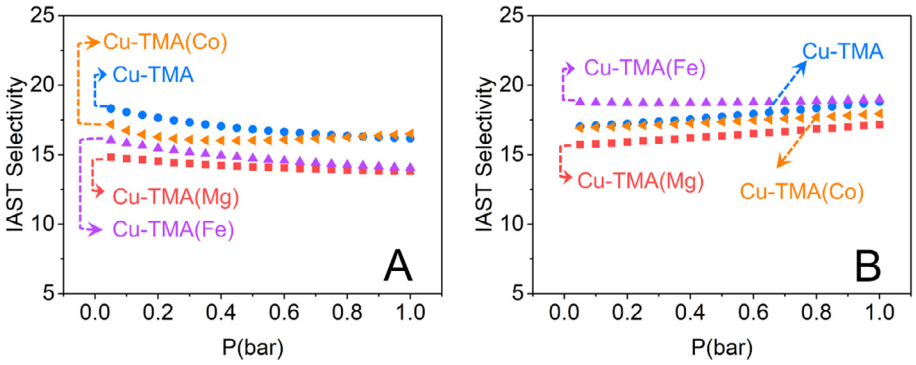

Fig. 8. IAST predicted CO_2/N_2 selectivity factors at (A) 273 K and (B) 298 K.

TMA(Co) (21.9 kJ/mol). This indicates that the interaction between preliminary CO_2 molecules and Cu is stronger than other substituting metal atoms. Typically, there are two steps involved in the adsorption of CO_2 in MOFs, including (1) direct contact of CO_2 with metal sites in initial stages and (2) pore filling at higher loadings [12]. Generally, the adsorption heat is higher in the first step, which is the case for both Cu-TMA and Cu-TMA(Mg) here. In particular, with increased CO_2 loading, the Qst of CO_2 adsorption in Cu-TMA fell to ~22.8 kJ/mol as a result of increased adsorption coverage. Cu-TMA(Mg) also showed decreasing Qst values at higher CO_2 loading (> 4.0 mmol/g). In contrast, in the cases of Cu-TMA(Fe) and Cu-TMA(Co), the Qst values showed overall increasing trends with increased CO_2 loading, which might be associated with the enhanced CO_2-CO_2 interaction [52,53].

Despite the heterogeneous adsorption sites in Cu-TMA, the most preferable adsorption sites for CO_2 were demonstrated to be the coordinatively unsaturated metal sites (CUS) [6]. In addition, the major bonding interaction stemmed from electrostatic effects, leading to CO_2 polarization (i.e., charge accumulation on O atom adjacent to CUS) and lower-energy CO_2 states [19]. Other minor contributions to the CO_2 adsorption include the van der Waals interactions [12,54]. To obtain additional insights, DFT computation was performed regarding the effects of metal substitution on the geometry and position of the adsorbed CO_2 molecule, from which the bond angle distortion and bond length of the CO_2 molecule will be obtained and can be used as another indicator of the interaction between CO_2 and the adsorption metal sites. Specifically, four model MOF structures were constructed and optimized, including the Cu-TMA primitive cell and the modified Cu-TMA primitive cells with two Cu atoms substituted with Fe, Co, and Mg, respectively. One optimized CO_2 molecule was placed in each framework adjacent to the metal substitution site. Subsequently, the geometries of primitive cells with the CO_2 molecules were optimized. The as-obtained results were shown in Figs. 10 and 11. The adsorbed CO_2 molecules in the Cu-TMA and all other bimetallic MOFs exhibited head-on configuration to the metal sites, consistent with previous reports [12,55]. Notably, the substituting metals had a significant effect on both the position and configuration of the adsorbed CO_2 molecule. For the bare Cu-TMA, the adsorbed CO_2 molecule exhibits marginal bond bending (179.370°), which agrees well with the results in a prior study [54]. The bond bending is due to the electrostatic interaction between CO_2 and the adsorption metal sites. Given such a small bond angle distortion, the

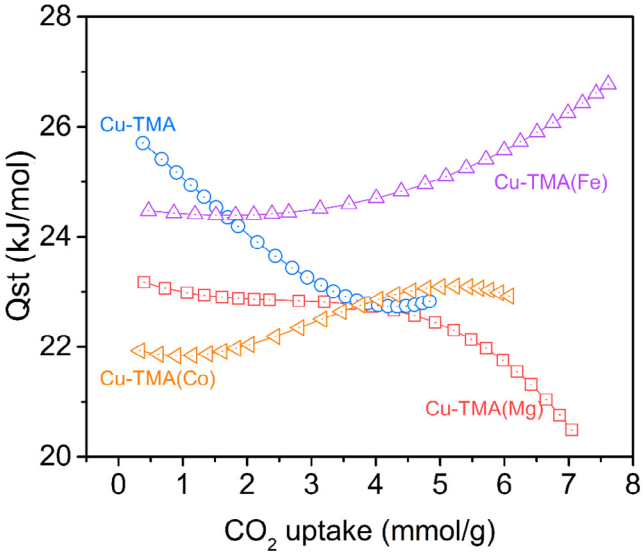

Fig. 9. Dependence of isosteric heat of adsorption on CO_2 uptake.

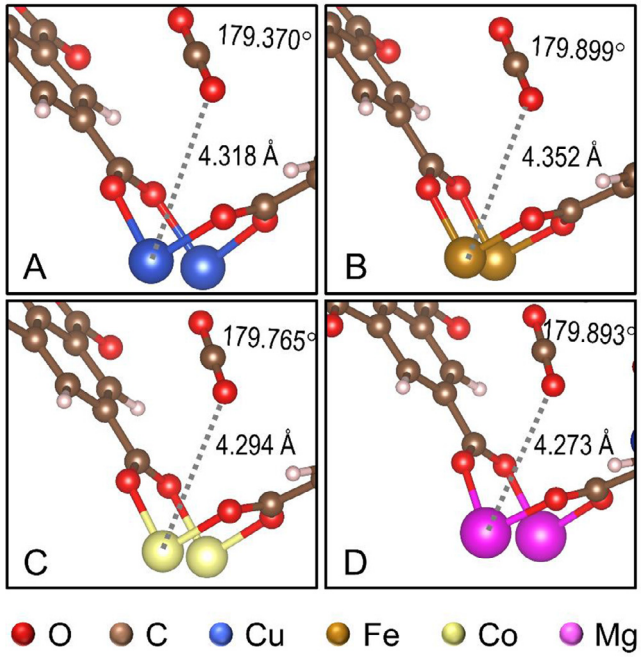

Fig. 10. DFT simulations of the interactions between CO_2 and metal centers in (A) Cu-TMA, (B) Cu-TMA(Fe), (C) Cu-TMA(Co), and (D) Cu-TMA(Mg).

adsorption of CO_2 inside Cu-TMA is dominated by physical adsorption.

Notably, less bond bending was observed for CO_2 molecules adsorbed in Cu-TMA(Fe) (179.899°), Cu-TMA(Co) (179.765°), and Cu-TMA(Mg) (179.893°). In particular, the O═C═O bond angle exhibits a negative correlation with the electronegativity (Pauling scale) of the adsorbing metals (Fig. 11). Meanwhile, asymmetric C═O bond lengths were observed for the adsorbed CO_2. As shown in Fig. S2, the C═O bond adjacent to the metal ion was more stretched than the one away from the metal ion. Overall, the average C═O bond lengths in CO_2 tend to increase with increasing electronegativity of the interacting metals (Fig. 11). The electronegativity is a property that can be used to compare the abilities of atoms to attract shared electron pairs. More specifically, during the CO_2 adsorption process, the lone pair electrons from the HOMO of CO_2 will be donated to the unsaturated electronic states of the metal as a result of electrostatic interaction [19].

Here, Cu has the largest electronegativity and thus has the strongest ability to attract the shared electron pair towards itself, which could lead to the highest O═C═O bond angle distortion and large C═O bond length (Fig. 11), subsequently resulting in the strongest interaction with CO_2. This agrees well with the experimental result that the highest isosteric heat of adsorption was obtained with bare Cu-TMA during the initial adsorption stage (Fig. 9). Meanwhile, the distortion degree of the O═C═O bond angle (Fig. 11) also correlated with the CO_2/N_2 selectivity at 273 K (Fig. 8A). In particular, the metal site with larger electronegativity induced higher distortion degree (Fig. 11) (i.e., higher electrostatic interaction), which caused higher CO_2/N_2 selectivity at 273 K (Fig. 8A). On the other hand, smaller electronegativity of the substituting metals (i.e., Mg, Fe, and Co) would provide Cu-TMA with adjustable CO_2 adsorption properties (e.g., isosteric heat of adsorption, Fig. 9), which is critical for the regeneration process after the adsorption.

3.4. Dynamic CO_2 adsorption

Additional analysis was conducted with the *in situ* DRIFTS to gain further information regarding the CO_2 adsorption sites and kinetics under the dynamic flow conditions. As shown in Fig. 12A and B, the physically adsorbed CO_2 molecules in both Cu-TMA and Cu-TMA(Fe) exhibited two characteristic peaks at ~2340 cm^{-1} and ~2360 cm^{-1}, all of which are attributed to the CO_2 molecules interacting with metals and functional groups, respectively [56]. Notably, higher peaks were observed at 2340 cm^{-1} for pristine Cu-TMA, while for Cu-TMA(Fe), the peak at 2360 cm^{-1} is prominent, suggesting that the metal sites in Cu-TMA play a more critical role in CO_2 adsorption than those in Cu-TMA(Fe). This finding is well consistent with DFT results shown in Figs. 10 and 11. Meanwhile, the variations in adsorption sites also partially explained the differences in isosteric heat of adsorption between Cu-TMA and Cu-TMA(Fe) (Fig. 9). The area under the peaks (from 2250 cm^{-1} to 2450 cm^{-1}) is positively correlated with the amount of adsorbed CO_2 molecules, based on which, the CO_2 adsorption dynamics were obtained (Fig. 12C). As shown in Fig. 12C, similar CO_2 adsorption rates were observed for Cu-TMA and Cu-TMA(Fe). Generally, CO_2 adsorption is an exothermic process, which is thermodynamically driven by the partial pressure of CO_2 [57]. Therefore, temperature swing adsorption (TSA) is a promising method to regenerate the samples given their good thermal stability as demonstrated via TGA measurements (Fig. 4). As an example, the reusability of the Cu-TMA(Fe) was analyzed by using *in situ* DRIFTS, where the areas under the peaks from 2250 cm^{-1} to 2450 cm^{-1} were continuously recorded to obtain the relative amount of adsorbed CO_2 molecules during the adsorption/desorption cycles. As shown in Fig. 12D, the CO_2 molecules desorbed from Cu-TMA (Fe) very quickly during the heating process (~2 min). Cu-TMA(Fe) still maintained more than 85.1% of its original CO_2 adsorption in the 5th adsorption/desorption cycle, which demonstrates the good reusability of the Fe-substituted Cu-TMA. The slightly decreased adsorption capacity might be related to the CO_2 residuals inside the framework after the desorption, causing additional diffusion resistances to the subsequent adsorption of CO_2 [58]. It should be noted that, with a longer desorption duration and/or regeneration techniques, the remaining CO_2 residuals would be completely removed, which could give rise to better reusability of the samples.

4. Conclusions

With the aid of the microdroplet-based spray system, a series of bimetallic MOFs were successfully prepared, including Cu-TMA(Fe), Cu-TMA(Co), Cu-TMA(Mg), Cu-TMA(Al), and Cu-TPA(Fe). Detailed characterization was conducted to analyze the effects of the secondary metal sites on the parent MOF's properties (e.g., crystalline structure, surface chemistry, surface area, porosity, and thermal stability). The results showed that, during the synthesis process, the secondary metal ions could be incorporated into the parent MOFs by interacting with the

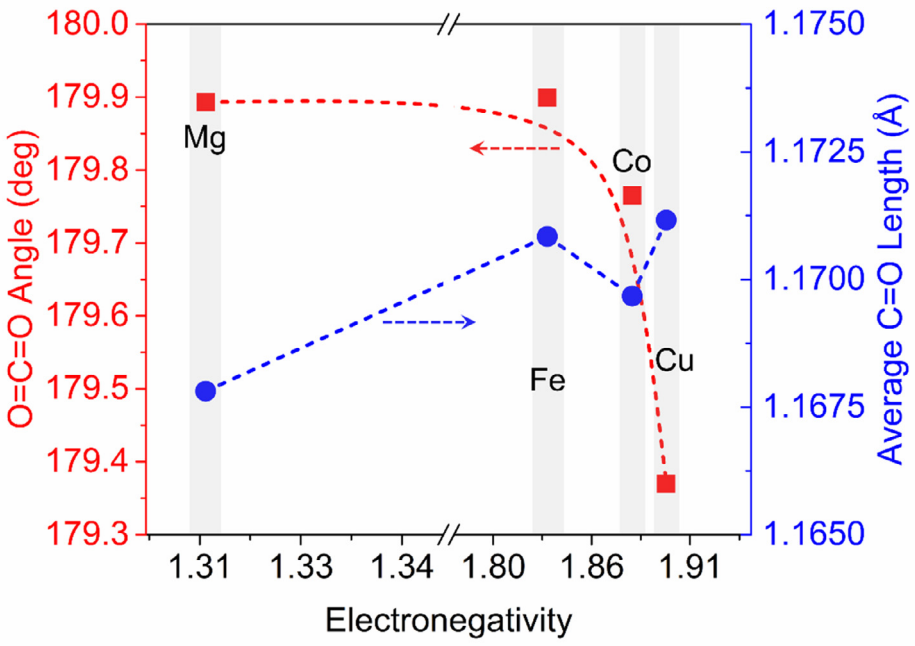

Fig. 11. O═C═O bond angles and average C═O bond lengths for the adsorbed CO_2 as a function of electronegativity (Pauling scale) of the interacting metal sites.

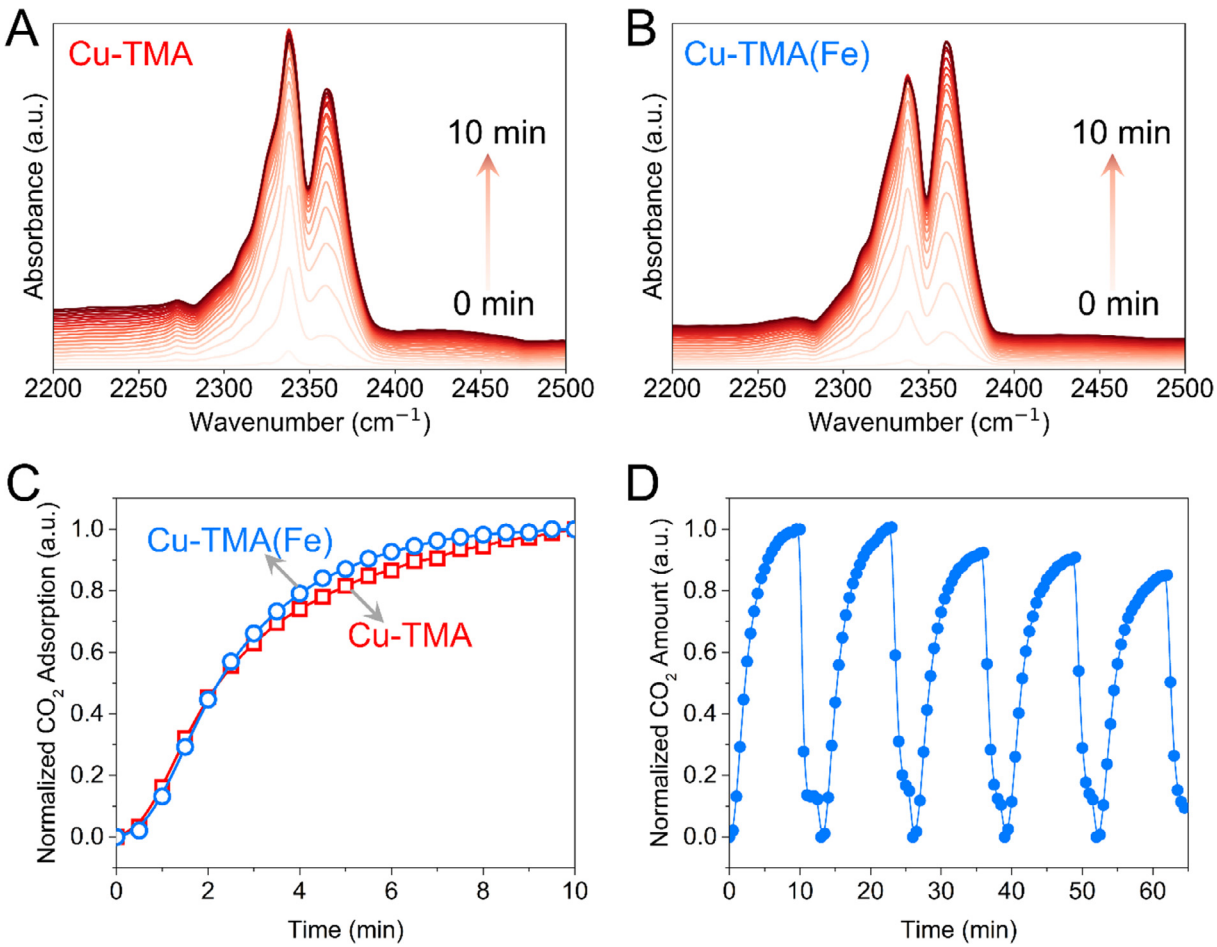

Fig. 12. DRIFT spectra of adsorbed CO_2 on (A) Cu-TMA and (B) Cu-TMA(Fe) from 0 min to 10 min; (C) CO_2 adsorption kinetics; (D) five cycles of CO_2 adsorption/desorption on Cu-TMA(Fe). Note: (1) the Fe/Cu ratio in the precursor for this Cu-TMA(Fe) is 0.3; (2) desorption conditions: purging gas: helium flow (30 ccm), temperature: 150 °C.

ligands and forming M-O bonds. A small amount of secondary metal ions would not damage the crystalline structures but could increase the BET surface areas to a certain extent, which might be attributed to the unit cell expansion induced by metal substitution. Interestingly, the pore volumes of the bimetallic MOFs exhibited a positive relationship with the atomic radii of the secondary metal sites. An additional gas sorption measurement was carried out with CO_2 and N_2 at various temperatures (i.e., 273 K and 298 K), with which the impact of secondary metal sites on gas adsorption capacity and selectivity was analyzed. In particular, the introduction of the secondary metal sites would alter the performances of MOFs in gas adsorption capacity, isosteric heat of adsorption, and CO_2/N_2 selectivity. Clues provided by DFT simulation indicate that C═O bond lengths and O═C═O bond angles for the adsorbed CO_2 have a great dependence on the electronegativity of the interacting metal sites, which might account for the aforementioned variations in sorption performances. Overall, partial substitution of the metals in MOFs offers great potentials for CO_2 capture and provides a cost-effective method for the sorbent regeneration.

5. Associated content

SEM Images of Representative Cu-TMA(Fe) Products; CO_2/N_2 Adsorption Selectivity; C═O Bond Lengths of Adsorbed CO_2.

Declaration of Competing Interest

The authors declare that they have no known competing financial interests or personal relationships that could have appeared to influence the work reported in this paper

Acknowledgment

The authors are grateful to the National Science Foundation (CMMI-1727553) for financial support.

Appendix A. Supplementary data

Supplementary data to this article can be found online at https://doi.org/10.1016/j.cej.2019.122825.

References

[1] National Oceanic and Atmospheric Administration, Trends in Atmospheric Carbon Dioxide, URL: https://www.esrl.noaa.gov/gmd/ccgg/trends/, last accessed: 08/19/2019.
[2] H.R. Abid, H. Tian, H.-M. Ang, M.O. Tade, C.E. Buckley, S. Wang, Nanosize Zr-metal organic framework (UiO-66) for hydrogen and carbon dioxide storage, Chem. Eng. J. 187 (2012) 415–420.
[3] C.-M. Lu, J. Liu, K. Xiao, A.T. Harris, Microwave enhanced synthesis of MOF-5 and its CO_2 capture ability at moderate temperatures across multiple capture and release cycles, Chem. Eng. J. 156 (2010) 465–470.
[4] J.-R. Li, Y. Ma, M.C. McCarthy, J. Sculley, J. Yu, H.-K. Jeong, P.B. Balbuena, H.-C. Zhou, Carbon dioxide capture-related gas adsorption and separation in metal-organic frameworks, Coord. Chem. Rev. 255 (2011) 1791–1823.
[5] J.-R. Li, R.J. Kuppler, H.-C. Zhou, Selective gas adsorption and separation in metal–organic frameworks, Chem. Soc. Rev. 38 (2009) 1477–1504.
[6] J. Yu, L.-H. Xie, J.-R. Li, Y. Ma, J.M. Seminario, P.B. Balbuena, CO_2 capture and separations using MOFs: computational and experimental studies, Chem. Rev. 117 (2017) 9674–9754.
[7] J.R. Karra, K.S. Walton, Molecular simulations and experimental studies of CO_2, CO, and N_2 adsorption in metal–organic frameworks, J. Phys. Chem. C 114 (2010) 15735–15740.
[8] Q. Yang, C. Zhong, J.-F. Chen, Computational study of CO_2 storage in metal–organic frameworks, J. Phys. Chem. C 112 (2008) 1562–1569.
[9] T. Devic, F. Salles, S. Bourrelly, B. Moulin, G. Maurin, P. Horcajada, C. Serre, A. Vimont, J.-C. Lavalley, H. Leclerc, G. Clet, M. Daturi, P.L. Llewellyn, Y. Filinchuk, G. Férey, Effect of the organic functionalization of flexible MOFs on the adsorption of CO_2, J. Mater. Chem. 22 (2012) 10266–10273.
[10] V. Gargiulo, M. Alfè, F. Raganati, L. Lisi, R. Chirone, P. Ammendola, BTC-based metal-organic frameworks: correlation between relevant structural features and CO_2 adsorption performances, Fuel 222 (2018) 319–326.
[11] X.-J. Hou, P. He, H. Li, X. Wang, Understanding the adsorption mechanism of C_2H_2, CO_2, and CH_4 in isostructural metal-organic frameworks with coordinatively unsaturated metal sites, J. Phys. Chem. C 117 (2013) 2824–2834.
[12] D. Yu, A.O. Yazaydin, J.R. Lane, P.D.C. Dietzel, R.Q. Snurr, A combined experimental and quantum chemical study of CO_2 adsorption in the metal–organic framework CPO-27 with different metals, Chem. Sci. 4 (2013) 3544–3556.
[13] W. Morris, N. He, K.G. Ray, P. Klonowski, H. Furukawa, I.N. Daniels, Y.A. Houndonougbo, M. Asta, O.M. Yaghi, B.B. Laird, A combined experimental-computational study on the effect of topology on carbon dioxide adsorption in zeolitic imidazolate frameworks, J. Phys. Chem. C 116 (2012) 24084–24090.
[14] A.Ö. Yazaydın, A.I. Benin, S.A. Faheem, P. Jakubczak, J.J. Low, R.R. Willis, R.Q. Snurr, Enhanced CO_2 adsorption in metal-organic frameworks via occupation of open-metal sites by coordinated water molecules, Chem. Mater. 21 (2009) 1425–1430.
[15] B. Wang, H. Huang, X.-L. Lv, Y. Xie, M. Li, J.-R. Li, Tuning CO_2 selective adsorption over N_2 and CH_4 in UiO-67 analogues through ligand functionalization, Inorg. Chem. 53 (2014) 9254–9259.
[16] P. Nugent, Y. Belmabkhout, S.D. Burd, A.J. Cairns, R. Luebke, K. Forrest, T. Pham, S. Ma, B. Space, L. Wojtas, M. Eddaoudi, M.J. Zaworotko, Porous materials with optimal adsorption thermodynamics and kinetics for CO_2 separation, Nature 495 (2013) 80.
[17] E.D. Bloch, D. Britt, C. Lee, C.J. Doonan, F.J. Uribe-Romo, H. Furukawa, J.R. Long, O.M. Yaghi, Metal insertion in a microporous metal − organic framework lined with 2,2′-bipyridine, J. Am. Chem. Soc. 132 (2010) 14382–14384.
[18] J. An, N.L. Rosi, Tuning MOF CO_2 adsorption properties via cation exchange, J. Am. Chem. Soc. 132 (2010) 5578–5579.
[19] H.S. Koh, M.K. Rana, J. Hwang, D.J. Siegel, Thermodynamic screening of metal-substituted MOFs for carbon capture, PCCP 15 (2013) 4573–4581.
[20] X. Yang, Q. Xu, Bimetallic metal-organic frameworks for gas storage and separation, Cryst. Growth Des. 17 (2017) 1450–1455.
[21] J.A. Botas, G. Calleja, M. Sánchez-Sánchez, M.G. Orcajo, Effect of Zn/Co ratio in MOF-74 type materials containing exposed metal sites on their hydrogen adsorption behaviour and on their band gap energy, Int. J. Hydrogen Energy 36 (2011) 10834–10844.
[22] J.A. Botas, G. Calleja, M. Sánchez-Sánchez, M.G. Orcajo, Cobalt doping of the MOF-5 framework and its effect on gas-adsorption properties, Langmuir 26 (2010) 5300–5303.
[23] F. Nouar, T. Devic, H. Chevreau, N. Guillou, E. Gibson, G. Clet, M. Daturi, A. Vimont, J.M. Grenèche, M.I. Breeze, R.I. Walton, P.L. Llewellyn, C. Serre, Tuning the breathing behaviour of MIL-53 by cation mixing, Chem. Commun. 48 (2012) 10237–10239.
[24] M.A. Gotthardt, R. Schoch, S. Wolf, M. Bauer, W. Kleist, Synthesis and characterization of bimetallic metal–organic framework Cu–Ru-BTC with HKUST-1 structure, Dalton Trans. 44 (2015) 2052–2056.
[25] A. Schejn, A. Aboulaich, L. Balan, V. Falk, J. Lalevée, G. Medjahdi, L. Aranda, K. Mozet, R. Schneider, Cu^{2+}-doped zeolitic imidazolate frameworks (ZIF-8): efficient and stable catalysts for cycloadditions and condensation reactions, Catal. Sci. Technol. 5 (2015) 1829–1839.
[26] Y. Kim, S. Das, S. Bhattacharya, S. Hong, M.G. Kim, M. Yoon, S. Natarajan, K. Kim, Metal-ion metathesis in metal-organic frameworks: a synthetic route to new metal-organic frameworks, Chem.-Eur. J. 18 (2012) 16642–16648.
[27] Z. Zhou, L. Mei, C. Ma, F. Xu, J. Xiao, Q. Xia, Z. Li, A novel bimetallic MIL-101(Cr, Mg) with high CO_2 adsorption capacity and CO_2/N_2 selectivity, Chem. Eng. Sci. 147 (2016) 109–117.
[28] X. He, W.-N. Wang, Rational design of efficient semiconductor-based photocatalysts via microdroplets: a review, KONA Powder Part. J. 36 (2019) 201–214.
[29] X. He, C. Yang, D. Wang, S.E. Gilliland Iii, D.-R. Chen, W.-N. Wang, Facile synthesis of ZnO@ZIF core-shell nanofibers: crystal growth and gas adsorption, CrystEngComm 19 (2017) 2445–2450.
[30] J. Hutter, M. Iannuzzi, F. Schiffmann, J. VandeVondele, cp2k: atomistic simulations of condensed matter systems, Wiley Interdisciplinary Rev.: Comput. Mol. Sci. 4 (2014) 15–25.
[31] J.P. Perdew, K. Burke, M. Ernzerhof, Generalized gradient approximation made simple, Phys. Rev. Lett. 77 (1996) 3865–3868.
[32] S. Grimme, Semiempirical GGA-type density functional constructed with a long-range dispersion correction, J. Comput. Chem. 27 (2006) 1787–1799.
[33] J. VandeVondele, J. Hutter, Gaussian basis sets for accurate calculations on molecular systems in gas and condensed phases, J. Chem. Phys. 127 (2007) 114105.
[34] S. Goedecker, M. Teter, J. Hutter, Separable dual-space Gaussian pseudopotentials, Phys. Rev. B 54 (1996) 1703–1710.
[35] X. He, Z. Gan, S. Fisenko, D. Wang, H.M. El-Kaderi, W.-N. Wang, Rapid formation of metal-organic frameworks (MOFs) based nanocomposites in microdroplets and their applications for CO_2 photoreduction, ACS Appl. Mater. Interfaces 9 (2017) 9688–9698.
[36] W.N. Wang, I.W. Lenggoro, K. Okuyama, Preparation of nanoparticles by spray routes, in: H.S. Nalwa (Ed.), Encyclopedia of Nanoscience and Nanotechnology, American Scientific Publishers, 2011, pp. 435–458.
[37] X. Song, M. Oh, M.S. Lah, Hybrid bimetallic metal-organic frameworks: modulation of the framework stability and ultralarge CO_2 uptake capacity, Inorg. Chem. 52 (2013) 10869–10876.
[38] N.A.A. Sani, W.J. Lau, A.F. Ismail, Polyphenylsulfone-based solvent resistant nanofiltration (SRNF) membrane incorporated with copper-1,3,5-benzenetricarboxylate (Cu-BTC) nanoparticles for methanol separation, RSC Adv. 5 (2015) 13000–13010.
[39] H. Zhang, R. Xiao, M. Song, D. Shen, J. Liu, Hydrogen production from bio-oil by chemical looping reforming, J. Therm. Anal. Calorim. 115 (2014) 1921–1927.
[40] V. Jabbari, J.M. Veleta, M. Zarei-Chaleshtori, J. Gardea-Torresdey, D. Villagrán, Green synthesis of magnetic MOF@GO and MOF@CNT hybrid nanocomposites

with high adsorption capacity towards organic pollutants, Chem. Eng. J. 304 (2016) 774–783.
[41] R. Kaur, A. Kaur, A. Umar, W.A. Anderson, S.K. Kansal, Metal organic framework (MOF) porous octahedral nanocrystals of Cu-BTC: Synthesis, properties and enhanced adsorption properties, Mater. Res. Bull. 109 (2019) 124–133.
[42] M.R. Azhar, H.R. Abid, H. Sun, V. Periasamy, M.O. Tadé, S. Wang, One-pot synthesis of binary metal organic frameworks (HKUST-1 and UiO-66) for enhanced adsorptive removal of water contaminants, J. Colloid Interface Sci. 490 (2017) 685–694.
[43] H. Liu, P. Li, B. Lu, Y. Wei, Y. Sun, Transformation of ferrihydrite in the presence or absence of trace Fe(II): The effect of preparation procedures of ferrihydrite, J. Solid State Chem. 182 (2009) 1767–1771.
[44] A.-N.A. El-Hendawy, Variation in the FTIR spectra of a biomass under impregnation, carbonization and oxidation conditions, J. Anal. Appl. Pyrolysis 75 (2006) 159–166.
[45] X. Hu, C. Li, X. Lou, Q. Yang, B. Hu, Hierarchical CuO octahedra inherited from copper metal–organic frameworks: high-rate and high-capacity lithium-ion storage materials stimulated by pseudocapacitance, J. Mater. Chem. A 5 (2017) 12828–12837.
[46] H. Niu, S. Liu, Y. Cai, F. Wu, X. Zhao, MOF derived porous carbon supported Cu/Cu_2O composite as high performance non-noble catalyst, Microporous Mesoporous Mater. 219 (2016) 48–53.
[47] X. Li, H. Liu, X. Jia, G. Li, T. An, Y. Gao, Novel approach for removing brominated flame retardant from aquatic environments using Cu/Fe-based metal-organic frameworks: a case of hexabromocyclododecane (HBCD), Sci. Total Environ. 621 (2018) 1533–1541.
[48] J. Bae, J.-W. Jung, H.Y. Park, C.-H. Cho, J. Park, Oxygen plasma treatment of HKUST-1 for porosity retention upon exposure to moisture, Chem. Commun. 53 (2017) 12100–12103.
[49] D.F. Sava Gallis, M.V. Parkes, J.A. Greathouse, X. Zhang, T.M. Nenoff, Enhanced O_2 selectivity versus N_2 by partial metal substitution in Cu-BTC, Chem. Mater. 27 (2015) 2018–2025.
[50] N. Huang, X. Chen, R. Krishna, D. Jiang, Two-dimensional covalent organic frameworks for carbon dioxide capture through channel-wall functionalization, Angew. Chem. Int. Ed. 54 (2015) 2986–2990.
[51] K. Sumida, D.L. Rogow, J.A. Mason, T.M. McDonald, E.D. Bloch, Z.R. Herm, T.-H. Bae, J.R. Long, Carbon dioxide capture in metal-organic frameworks, Chem. Rev. 112 (2012) 724–781.
[52] X. He, W.-N. Wang, Pressure-regulated synthesis of Cu(TPA)·(DMF) in microdroplets for selective CO_2 adsorption, Dalton Trans. 48 (2019) 1006–1016.
[53] J.A. Mason, K. Sumida, Z.R. Herm, R. Krishna, J.R. Long, Evaluating metal–organic frameworks for post-combustion carbon dioxide capture via temperature swing adsorption, Energy Environ. Sci. 4 (2011) 3030–3040.
[54] H. Wu, J.M. Simmons, G. Srinivas, W. Zhou, T. Yildirim, Adsorption sites and binding nature of CO_2 in prototypical metal–organic frameworks: a combined neutron diffraction and first-principles study, J. Phys. Chem. Lett. 1 (2010) 1946–1951.
[55] J. Park, H. Kim, S.S. Han, Y. Jung, Tuning metal-organic frameworks with open-metal sites and its origin for enhancing CO_2 affinity by metal substitution, J. Phys. Chem. Lett. 3 (2012) 826–829.
[56] X. He, W.-N. Wang, Synthesis of Cu-trimesic acid/Cu-1,4-benzenedioic acid via microdroplets: role of component compositions, Cryst. Growth Des. 19 (2019) 1095–1102.
[57] F. Raganati, M. Alfe, V. Gargiulo, R. Chirone, P. Ammendola, Isotherms and thermodynamics of CO_2 adsorption on a novel carbon-magnetite composite sorbent, Chem. Eng. Res. Des. 134 (2018) 540–552.
[58] F. Raganati, M. Alfe, V. Gargiulo, R. Chirone, P. Ammendola, Kinetic study and breakthrough analysis of the hybrid physical/chemical CO_2 adsorption/desorption behavior of a magnetite-based sorbent, Chem. Eng. J. 372 (2019) 526–535.

Bimetallic Metal-Organic Frameworks (MOFs) Synthesized Using the Spray Method for Tunable CO_2 Adsorption

*Xiang He, Da-Ren Chen, and Wei-Ning Wang**

Department of Mechanical and Nuclear Engineering, Virginia Commonwealth University, Richmond, Virginia 23219, United States

Corresponding Author

*Wei-Ning Wang: Tel: 1-(804) 827-4306; Fax: 1-(804) 827-7030; Email: wnwang@vcu.edu

S1. SEM Images of Representative Cu-TMA(Fe) Products

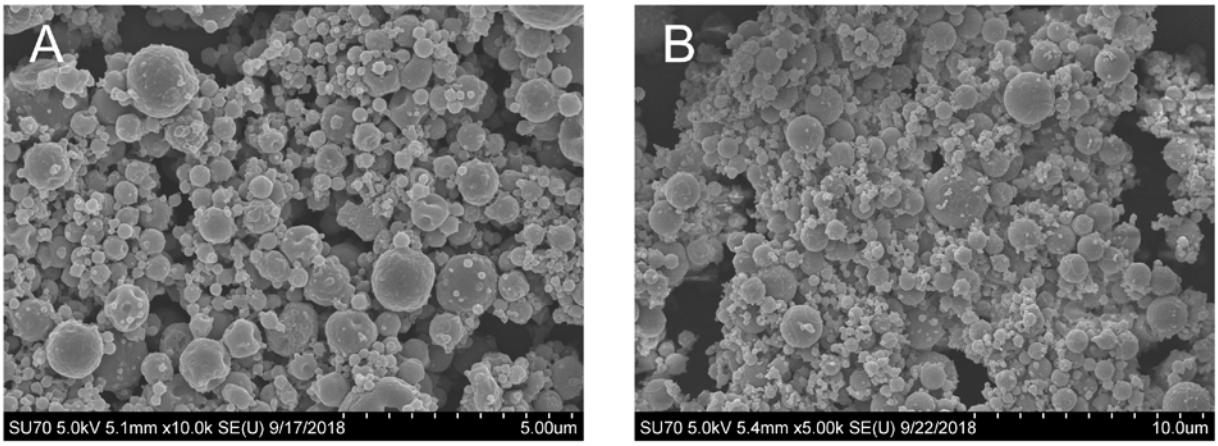

Figure S1. SEM images of Cu-TMA(Fe) synthesized with various Fe/Cu (mol/mol) in precursors: (A) 0.1 and (B) 1.

S2. CO_2/N_2 Adsorption Selectivity

Table S1. CO_2/N_2 adsorption selectivity.

	273 K		298 K	
	IAST	Initial Slope	IAST	Initial Slope
Cu-TMA	16.2-18.3	13.6	17.0-18.8	14.2
Cu-TMA(Fe)	14.0-16.0	13.9	18.7-19.0	18.3
Cu-TMA(Co)	16.0-17.2	14.5	16.9-17.9	17.0
Cu-TMA(Mg)	13.8-14.8	13.5	15.7-17.2	15.7

S3. C=O Bond Lengths of Adsorbed CO_2

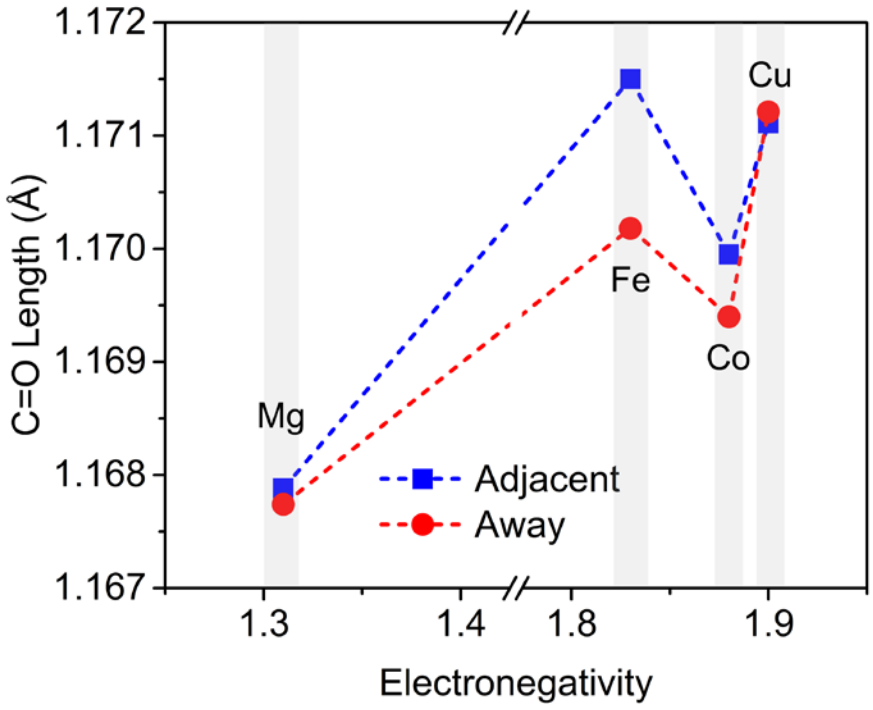

Figure S2. C=O bond lengths of adsorbed CO_2 as a function of the electronegativity (Pauling scale) of the interacting metal sites. Blue: the C=O bond adjacent to the metal site; Red: the C=O bond away from the metal site.